

Multi-objective Optimization of Combined Internal Components with a Vortex Stabilizer and Apex Cone for Performance Improvement of Cyclone Separator

Z. Zhang^{1,2,3}, H. R. Qin^{1,2,3}, Y. J. Zhao^{1,2}, J. Li^{1,2}, H. J. Pan^{1,2}, C. H. Hu^{1,2} and L. Liu^{1,2,3†}

¹ School of Mechanical Engineering and Rail Transit, Changzhou University, Changzhou 213164, China

² Jiangsu Key Laboratory of Green Process Equipment, Changzhou University, Changzhou, 213164, China

³ Changzhou University, CNPC-CZU Innovation Alliance, 213164, China

†Corresponding Author Email: liulin@cczu.edu.cn

ABSTRACT

Multi-objective optimization of a cyclone with combined internal components, including a vortex stabilizer and apex cone, was studied for performance improvement. Response Surface Methodology (RSM) and Computational Particle Fluid Dynamics (CPFD) were employed to investigate the effects of four parameters: vortex stabilizer diameter D_H , apex cone bottom length D_S , position B_S , and height B_H on separation efficiency, pressure drop, and quality factor. The desirability function was used to determine the optimized structure. The results demonstrated that D_S primarily affected separation efficiency and quality factor, whereas D_H mainly influenced pressure drop. The reduction in these two parameters, as well as the decrease in B_S , contributed to performance enhancement relative to their original values. After optimizing, separation efficiency, pressure drop, and quality factor could be improved by 5.605 %, 0.910 % and 16.673 %, respectively, and D_H , D_S , B_S and B_H were recommended at 27.512, 115.354, -80.1099 and 109.317 mm, respectively. In contrast to the original cyclone, the optimized separator exhibited a more stable flow due to the lower vortex end and minor wall turbulent viscosity. Although static pressure increased, particle back-mixing was alleviated. Additionally, the extended particle flow descending distances and the enlarged effective passage area enhanced particle centrifugal force and decreased particle volume fraction, respectively, thereby improving separation efficiency. Finally, the optimized separator exhibited enhanced overall performance across various operating parameters.

Article History

Received December 12, 2024

Revised March 28, 2025

Accepted April 1, 2025

Available online June 3, 2025

Keywords:

Multi-objective optimization
Cyclone separator
Combined internal components
Response surface methodology
Computational particle fluid dynamic

1. INTRODUCTION

With the advantages of low cost, high flexibility, and virtually no maintenance, cyclone separators are widely used in natural gas dedusting, the petrochemical industry, and other fields (Bumrunghthaichan, 2023; Li et al., 2023a). Despite the widespread application of cyclone separators in industrial processes, achieving optimal performance characterized by high separation efficiency and minimal pressure drop remains a major challenge.

The effects of the basic structure of the cyclone on flow behavior and performance have been extensively investigated, including inlet duct length and angle (Wasilewski & Brar, 2019; Yao et al., 2021), vortex finder length and diameter (Wei et al., 2020; Zheng et al., 2022;), cylinder and cone shapes (Pandey & Brar, 2023), and dust

box dimensions (Elsayed et al., 2020). Previous research has improved the performance of cyclones to a certain extent; however, adjusting the existing structure increases cost and engineering efforts in industrial applications. Therefore, improving performance by adding internal components (vortex stabilizer, apex cone, etc.) without changing the original size of the cyclone has become a hotspot for scholars (He et al., 2019; Liang et al., 2023; Yang et al., 2023). Among these, vortex stabilizer and apex cone have attracted the attention of many researchers (Yang et al., 2019). Through experiments and Computational Fluid Dynamics (CFD) simulations, Duan et al. (2020) proved that changing the size of the vortex stabilizer could affect flow structure and, thus, cyclone performance. Guo et al. (2023) also reported that a vortex stabilizer enhanced flow stability and reduced the radial

NOMENCLATURE			
a	inlet height	\mathbf{u}_g	gas velocity vector
b	cylinder diameter	\mathbf{u}_p	particle velocity vector
B_H	apex cone height	v_{gas}	gas inlet velocity
B_S	apex cone position	Y	response
C_d	drag coefficient	Greek letters	
D	cylinder diameter	α	distance of each star point in CCD
D_B	dust box diameter	η	cyclone separation efficiency
D_C	cone tip diameter	δ	experimental error
D_H	vortex stabilizer diameter	β_0	regression coefficients for the offset term
D_S	apex cone bottom length	β_i	regression coefficients for the linear migration terms
D_p	drag function	β_{ii}	regression coefficients for the quadratic migration terms
D_X	gas outlet diameter	β_{ij}	regression coefficients for the interaction terms
du_p/dt	particle acceleration	μ_g	turbulent viscosity
\mathbf{F}	gas–solid drag force	ρ_g	gas density
\mathbf{g}	gravitational acceleration	ρ_p	particle density
k	factor number	$\boldsymbol{\tau}_g$	gas stress tensor
L_B	dust box length	$\boldsymbol{\tau}_p$	particle normal stress tensor
L_C	cylinder length	θ_{cp}	particle volume fraction
L_O	outlet pipe length	θ_g	gas volume fraction
L_V	vortex finder length	θ_p	particle volume fraction
m_p	particle inlet mass rate	Abbreviation	
N	design points	CCD	Central Composite Design
n	replication number	CPFD	Computational Particle Fluid Dynamics
p	gas pressure	LES	Large-Eddy Simulation
ΔP	cyclone pressure drop	MP-PIC	Multi-Phase Particle-in-Cell
q	cyclone quality factor	RSM	Response Surface Methodology
Re	Reynolds number		

pressure gradient but reduced centrifugal force in the central region. Zhang et al. (2023) further confirmed that installing an apex cone could improve swirl length, resulting in a lower pressure drop without a steep decline in separation efficiency. Despite these advancements, the combined application of internal components, such as vortex stabilizers and apex cones, has been barely explored to maximize separation efficiency and minimize pressure drop simultaneously.

Previous studies have primarily focused on the adjustment of individual structural parameters, with a notable lack of research on the interactions between multiple parameters. In recent years, the implementation and application of optimization techniques has increased. Design optimization of cyclone separators primarily involves mathematical optimization problems that aim to optimize multiple parameters and objective functions simultaneously (Tan et al., 2024). For example, Elsayed et al. (2020) applied an Artificial Neural Network (ANN) to study the influence of dust-box dimensions on cyclone performance. Khalili et al. (2023) used a Genetic Algorithm (GA) to explore the effect of geometric optimization of the cyclone separator on the flow field and performance parameters. Shastri et al. (2022) applied a GA to optimize the vortex finder diameter, length, height, conical segment, the cone tip diameter. The new model reduced the pressure drop by 40%. Among these methods, the Response Surface Methodology (RSM) has proven effective for cyclone separator optimization because it explores the complex interactions between multiple

parameters (Tang et al., 2023; Jiang et al., 2024). Kumar and Jha (2019) performed a multi-objective optimization of vortex finders using RSM and GA, and the results confirmed that the optimization structure performed better than the standard Stairmand model. Li et al. (2023b) utilized RSM to optimize wedge-shaped roof height, top diameter, and bottom diameter. Results indicated that modifying the wedge-shaped roof height and top diameter enhanced flow field and separation performance, whereas increasing the bottom diameter had the opposite effect. The optimal structure improved the separation efficiency by 4.2% compared with the original design, but the pressure drop increased by 11%. Li et al. (2020a) also conducted a multi-objective optimization of an axial-flow cyclone separator. Their investigation revealed that numerous parameters influenced the separation performance of the cyclone. Compared to the original design, the optimized design increased separation efficiency for 8 μm particles and pressure drop by 100% and 69.32%, respectively. Moreover, researchers have gradually introduced optimization technology into the study of internal components (Wasilewski et al., 2021; Dehdarinejad & Bayareh, 2023). Guo et al. (2022) slotted gaps on a vortex finder wall and proposed a multi-objective optimization using RSM and CFD. The optimized structure provided a separation efficiency increase of 4.32% and a Euler number reduction of 34.51% compared with the original structure. Previous studies primarily focused on optimizing the basic structure or individual internal components of cyclone separators.

However, comprehensive studies on the optimization of combined internal components and their effects on cyclone performance are limited.

In this study, the separation process of a cyclone separator with a vortex stabilizer and apex cone was simulated using Computational Particle Fluid Dynamics (CPFD). The vortex stabilizer diameter D_H , apex cone bottom length D_S , position B_S , and height B_H were optimized for performance improvement using RSM. First, the significance of each parameter on the responses (separation efficiency, pressure drop, and quality factor) was analyzed using Analysis of Variance (ANOVA). The effects of individual parameters and the interactions between different parameters on the responses were explored through response surface analysis. Subsequently, a desirability function approach was used to obtain an optimized structure. Finally, the gas flow field, along with particle volume fraction and trajectory, were compared and analyzed for the original and optimized structures, as well as their performances under varying operating parameters.

2. MODEL AND METHODOLOGY

2.1 Details of Cyclone Separator Geometry and Computational Grid

In this study, a cyclone separator with a vortex stabilizer and an apex cone was investigated based on the experimental structure proposed by Kosaki et al. (2015). The original structure of the cyclone is illustrated in Fig. 1(a), and its geometric dimensions are listed in Table 1. A

uniform Cartesian grid was employed for the simulations conducted in Barracuda, following recommendations from previous studies (Bandara et al., 2020). Mesh refinement is crucial for accurately capturing the computational domains of complex sections. Consequently, finer mesh elements were applied to the vortex finder wall and central up flow region, where the flow turbulence was most pronounced. The computational grid is shown in Fig. 1(b).

2.2 Mathematical Model

As a Eulerian–Lagrangian model, CPFD can calculate a significant number of real particles within gas–solid flows. The gas phase was treated as a continuum by solving the averaged Navier–Stokes equation, whereas the particle phase was represented as a discrete phase. The particle phase was coupled with the gas phase through drag force interactions based on the Multi-Phase Particle-in-Cell (MP-PIC) approach (Zhang et al., 2020). In the MP-PIC method, each particle is subjected to external forces such as fluid drag, gravity, and particle collisions.

2.2.1 Governing Equations

In the current study, the gas–solid cyclone was assumed to be isothermal and devoid of any reactions, therefore, both the energy and species transport equations were neglected. The gas was treated as an incompressible fluid, whereas the particles were modeled as Lagrangian computational particles. These particles were categorized as package particles based on their density and size, which helps reduce computational costs.

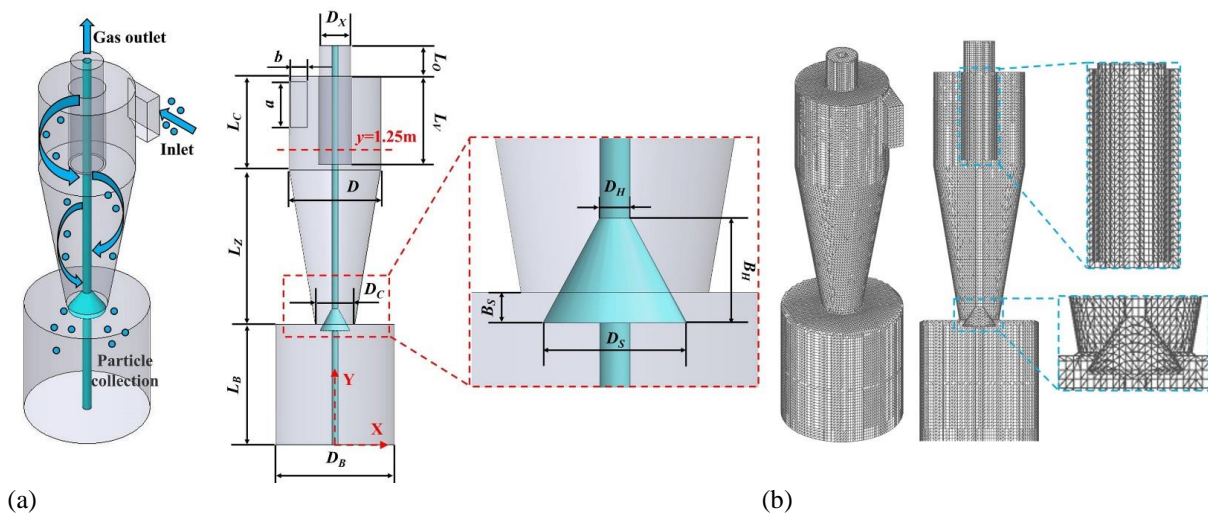


Fig. 1 (a) Original structure of cyclone separator; (b) computational grid

Table 1 Geometric dimensions ($D = 385 \text{ mm}$)

Parameters	Symbols	Dimensions	Parameters	Symbols	Dimensions
Gas outlet diameter	D_X	$0.34D$	Cylinder length	L_C	$1.02D$
Cone tip diameter	D_C	$0.43D$	Cone length	L_Z	$1.69D$
Dust box diameter	D_B	$1.30D$	Dust box length	L_B	$1.32D$
Vortex stabilizer diameter	D_H	$0.09D$	Outlet pipe length	L_O	$0.34D$
Apex cone bottom length	D_S	$0.39D$	Vortex finder length	L_V	$0.96D$
Apex cone position	B_S	$-0.07D$	Inlet height	a	$0.50D$
Apex cone height	B_H	$0.28D$	Inlet width	b	$0.18D$

For the gas phase, the continuity equation is:

$$\frac{\partial}{\partial t}(\theta_g \rho_g) + \nabla \cdot (\theta_g \rho_g \mathbf{u}_g) = 0 \quad (1)$$

where ρ_g is the gas density (kg/m³), \mathbf{u}_g is the gas velocity (m/s), and θ_g is the gas volume fraction.

The momentum equation for the gas phase is:

$$\frac{\partial}{\partial t}(\theta_g \rho_g \mathbf{u}_g) + \nabla \cdot (\theta_g \rho_g \mathbf{u}_g \mathbf{u}_g) = -\theta_g \nabla p - \mathbf{F} + \theta_g \rho_g \mathbf{g} + \nabla \cdot \boldsymbol{\tau}_g \quad (2)$$

where p is the gas pressure (Pa), $\boldsymbol{\tau}_g$ is the gas stress tensor (Pa), and \mathbf{g} is the gravitational acceleration (m/s²). The energy equation was not considered in the cold-state simulation. \mathbf{F} is the momentum exchange per unit volume between the gas and particle phases, and is calculated as follows:

$$\mathbf{F} = \iint fm \left(D_p (\mathbf{u}_g - \mathbf{u}_p) - \frac{\nabla p}{\rho_p} \right) dudm \quad (3)$$

where \mathbf{u}_p is the particle velocity (m/s), D_p is the drag function (kg/m³·s), and ρ_p is the particle density (kg/m³).

The turbulence model employed in the CPFD simulation was a Large-Eddy Simulation (LES). The fluid velocity and pressure were correlated using a semi-implicit pressure correction equation derived from the mass conservation equations. The solving method was the SIMPLE algorithm (Liu et al., 2023).

For the particle phase, the probability function f is introduced to describe the average number of particles per unit volume and is calculated using the following equation:

$$\frac{\partial f}{\partial t} + \nabla \cdot (\mathbf{u}_p f) + \nabla_{\mathbf{u}_p} \cdot \left(f \frac{d\mathbf{u}_p}{dt} \right) = 0 \quad (4)$$

where $d\mathbf{u}_p/dt$ is the particle acceleration (m/s²), which is described by:

$$\frac{d\mathbf{u}_p}{dt} = D_p (\mathbf{u}_g - \mathbf{u}_p) + \mathbf{g} - \frac{1}{\rho_p} \nabla p - \frac{1}{\theta_p \rho_p} \nabla \cdot \boldsymbol{\tau}_p \quad (5)$$

where θ_p is the particle volume fraction and $\boldsymbol{\tau}_p$ the particle normal stress tensor (N/m²). The four terms on the right-hand side of Eq. (5) represent the effects of drag, gravitational force, pressure gradient, and particle collision forces, respectively.

2.2.2 Drag Model

The drag coefficient is influenced by both particle properties and characteristics of the surrounding fluid. The Wen–Yu/Ergun model effectively accommodates a wide range of particle concentrations, from zero to maximum accumulation, while avoiding the numerical issues associated with sharp transitions or discontinuities. Owing to these advantages, the Wen–Yu/Ergun model was employed in the simulations (Ma et al., 2017).

The drag coefficient D_p in the formula is calculated by the following equation:

$$D_p = \begin{cases} D_{Wen-Yu} & \theta_p < 0.75\theta_{cp} \\ D_{Wen-Yu} + \frac{\theta_p - 0.85\theta_{cp}}{0.85\theta_{cp} - 0.75\theta_{cp}} (D_{Ergun} - D_{Wen-Yu}) & 0.75\theta_{cp} \leq \theta_p \leq 0.85\theta_{cp} \\ D_{Ergun} & \theta_p > 0.85\theta_{cp} \end{cases} \quad (6)$$

where θ_{cp} is the particle volume fraction; D_{Wen-Yu} and D_{Ergun} are the coefficients of the Wen–Yu and Ergun models (kg/m³·s), respectively, which can be calculated by the following equations:

Wen–Yu model:

$$D_{Wen-Yu} = \frac{3}{8} C_d \frac{\rho_g (\mathbf{u}_g - \mathbf{u}_p)}{\mu_g} \quad (7)$$

where μ_g is the turbulent viscosity (kg/m·s), and C_d is described by:

$$C_d = \begin{cases} \frac{24}{Re} \theta_g^{-2.65} & Re < 0.5 \\ \frac{24}{Re} \theta_g^{-2.65} (1 + 0.15 Re^{0.687}) & 0.5 \leq Re \leq 1000 \\ 0.44 \theta_g^{-2.65} & Re > 1000 \end{cases} \quad (8)$$

Ergun model:

$$D_{Ergun} = \frac{1}{2} \left(\frac{180\theta_p}{\theta_g Re} + 2 \right) \frac{\rho_f (\mathbf{u}_g - \mathbf{u}_p)}{\boldsymbol{\tau}_p \rho_p} \quad (9)$$

2.2.3 Solid Stress Model

Interparticle collisions were analyzed using the normal stress model in CPFD. Initially, the solid volume fraction is established by mapping the particle volume onto a grid. This solid volume fraction was then used to calculate the solid stress (Li et al., 2020b). The stress model was computed using the following equation:

$$\boldsymbol{\tau}_p = \frac{P_p \theta_p^\beta}{\max \left[(\theta_{cp} - \theta_p), \varepsilon (1 - \theta_p) \right]} \quad (10)$$

where P_p is a constant generally equal to 1. β is the model parameter recommended between 2 and 5, and ε is a small number on the order of 10⁻⁷ to remove the singularity at close packing.

2.3 Numerical Settings

In this study, commercial software Barracuda based on CPFD was used for simulations. The inlet medium consisted of air with a density of 1.2 kg/m³ and a velocity of 12 m/s. At the top, the outlet pipe was configured with the pressure outlet boundary set to atmospheric pressure. The mass flow rate of acrylic spherical particles was 0.01 kg/s, with a particle density of 1200 kg/m³. The particle

Table 2 Input parameters in the CPFD simulation

Gas-solid drag model		Wen–Yu/Ergun	
Close pack volume fraction	0.55	Pressure constant (Pa)	1
Collisional momentum redirection	40%	Beta constant	3
Normal-to-wall momentum retention	0.85	Epsilon constant	10^{-8}
Tangent-to-wall momentum retention	0.85	CFL number	0.8-1.5

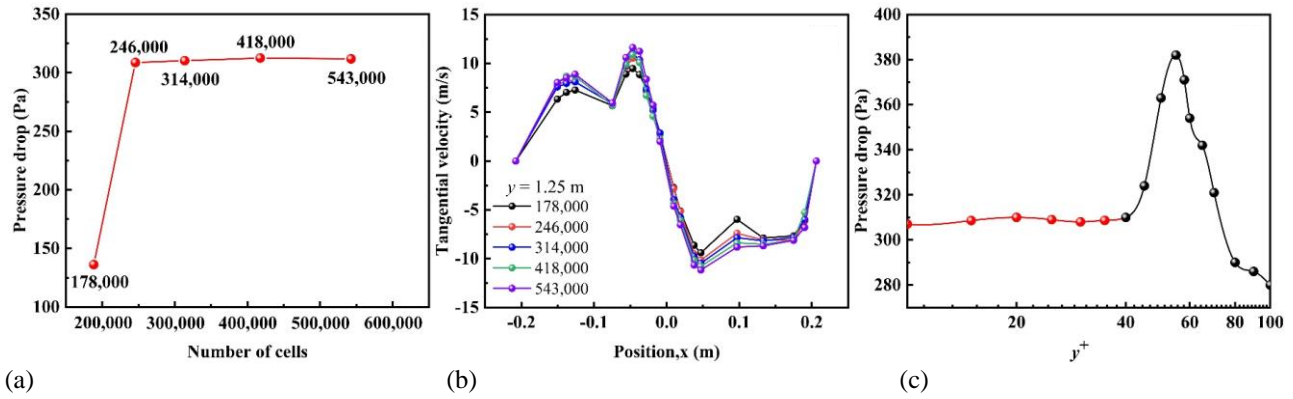


Fig. 2 Grid independence verification: (a) pressure drop, (b) tangential velocity at $y = 1.25$ m and (c) y^+ value

size range was between 1 and 10 μm , with a mass median diameter of 5 μm (Kosaki et al., 2015). A non-slip wall boundary condition was implemented.

To ensure computational efficiency and prevent divergence, the Courant-Friedrichs-Lewy (CFL) condition was set with a range of 0.8 to 1.5, as referenced in previous cyclone simulations (Bandara et al., 2019; Feng et al., 2025). Based on the range, an adaptive time-stepping algorithm was adopted, and 0.001 s was input as the upper limit for the time step recommended by Venkatesh (2020) and Yao (2024). During the calculation, if the CFL number experiences a significant deviation, the Barracuda solver can dynamically adjust the time step to maintain the CFL number within the above range (Ma et al., 2017). The other essential parameters used in the simulations are listed in Table 2.

2.4 Grid Independence and Model Validation

To ensure grid independence, five grids were selected (178,000, 246,000, 314,000, 418,000, 543,000). In the near-wall regions, finer meshes were generated with a growth ratio of 1.1 for the initial thirty layers. This approach was adopted to accurately capture the shear stress and velocity gradient within the boundary layer, where y^+ was approximately 35, which falls within the recommended range for LES used in a cyclone separator (Vakamalla & Mangadoddy, 2017). The verification of grid independence, based on pressure drop analysis, is illustrated in Fig. 2(a). The results indicate that the variation in pressure drop is less than 2% when the grid count exceeds 245,000. Furthermore, Fig. 2(b) depicts the tangential velocity distribution at $y = 1.25$ m for varying grid numbers. It is evident that the tangential velocities for grid numbers ranging from 245,000 to 542,000 are remarkably consistent, with discrepancies under 3%. This consistency suggests that a grid number of 245,000 is optimal. Additionally, the effect of y^+ was further verified based on the above settings in Fig. 2(c). The pressure drop

exhibits minimal changes until the y^+ value reaches 40, confirming that a y^+ value of 35, as utilized in this study, is indeed appropriate.

To ensure the reliability of the numerical calculation model, simulation results for the cyclone separator were compared with the experimental data (Morin et al., 2021), where IR is the inlet aspect ratio of height to width. As shown in Fig. 3, the maximum difference in separation efficiency is less than 1%, whereas the maximum difference in pressure drop is less than 13% under different normalized inlet solid loadings. These results indicate that the numerical results agree with the experimental data, suggesting that the numerical model can accurately predict flow characteristics and separation performance of cyclone separators.

3. MULTI-OBJECTIVE OPTIMIZATION

3.1 Response Surface Methodology (RSM)

RSM is a collection of statistical and mathematical methods that involves fitting empirical models to data and is widely used in product design, development, and optimization. The Central Composite Design (CCD) proposed by Box and Hunter is suitable for quadric surface fitting in RSM and is particularly effective for process optimization (Li et al., 2020b). The design points for a fully uniformly rotatable CCD are the sum of the cube, axial, and center points, which are expressed as (Altok et al., 2022):

$$N = k^2 + 2k + n \tag{11}$$

where k and n are the number of factors and replications at the center points, respectively. All factors were investigated at five levels ($-\alpha, -1, 0, 1, +\alpha$). The α value defines the distance of each star point from the center and CCD type, which is calculated as follows:

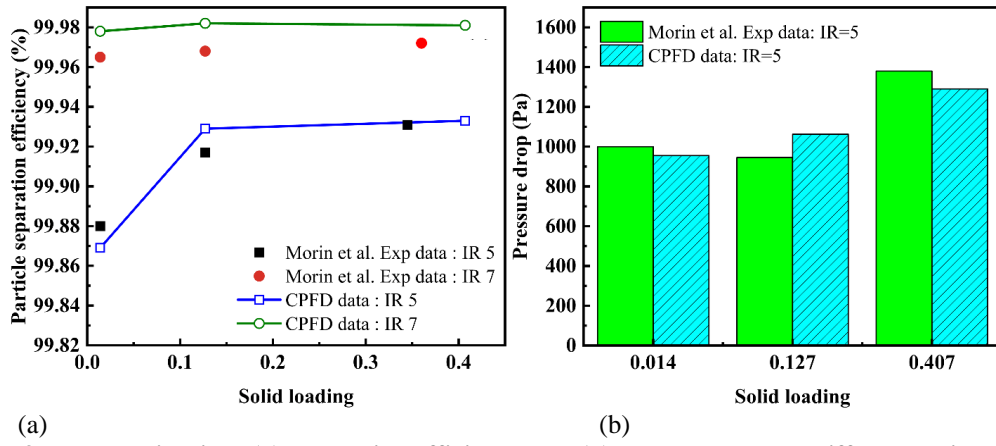


Fig. 3 Model validation: (a) separation efficiency and (b) pressure drop at different solid loadings

Table 3 Values and levels of the parameters

Parameters	$-\alpha$	(-1)	0	$(+1)$	$+\alpha$
A-Vortex stabilizer diameter D_H	$0.01D$	$0.05D$	$0.09D$	$0.13D$	$0.17D$
B-Apex cone bottom length D_S	$0.17D$	$0.23D$	$0.29D$	$0.35D$	$0.41D$
C-Apex cone position B_S	$-0.21D$	$-0.14D$	$-0.07D$	0	$0.07D$
D-Apex cone height B_H	$0.03D$	$0.18D$	$0.33D$	$0.48D$	$0.63D$

$$\alpha = 2^{1/4} \quad (12)$$

The quadratic-order model in the RSM-CCD illustrates the relationship between factors and response indicators and is expressed as follows (Li et al., 2020b):

$$Y = \beta_0 + \sum_{i=1}^k \beta_i x_i + \sum_{i=1}^k \beta_{ii} x_i^2 + \sum_{\substack{i=1 \\ i < j}}^k \beta_{ij} x_i x_j + \delta \quad (13)$$

where Y is the response, and β_0 , β_i , β_{ii} , and β_{ij} are the regression coefficients for the offset term, linear migration, quadratic migration, and interaction terms, respectively. Additionally, x_i and x_j are factors, and δ is the experimental error.

3.1.1 Central Composite Design (CCD)

The CCD evaluated separation efficiency η , pressure drop ΔP , and quality factor q of the cyclone separator as the three response indicators. These are defined as (Liang et al., 2023; Wang et al., 2023):

$$\eta = \frac{m_i - m_o}{m_i} \times 100\% \quad (14)$$

where m_i is the particle inlet mass (kg), and m_o is the particle outlet mass (kg).

$$\Delta P = P_I - P_O \quad (15)$$

where P_I is the inlet pressure (Pa), and P_O is the outlet pressure (Pa).

In this study, quality factor q was used to comprehensively evaluate separation performance by simultaneously considering the efficiency and pressure drop and was calculated as follows:

$$q = \frac{-\ln(1 - \eta/100)}{\Delta P} \quad (16)$$

where η is separation efficiency (%), and ΔP is pressure drop (KPa).

In this work, a four-factor, five-level CCD-RSM was utilized to investigate the effects of each parameter and their interactions on separation efficiency, pressure drop, and quality factor, while predicting the optimized high-performance structure. The Design-Expert software facilitates the regression analysis and optimization process.

In the CCD model, the value of α was set to $2^{1/4} = 2$, and a total of 30 runs were conducted, comprising 16 cubes, eight stars, and six center points. Table 3 lists the four parameters and their respective levels. The vortex stabilizer diameter D_H (A), apex cone bottom length D_S (B), apex cone position B_S (C), and apex cone height B_H (D) were identified as the response parameters. The negative sign associated with B_S indicates that the bottom of the apex cone is located within the dust box. The regression equations (Eq. 17–19) were derived from 30 simulation sets to establish correlations between the parameters and response values. The adequacy and significance of the regression models were evaluated using ANOVA. Individual parameter curves, 3D response surfaces, and contour plots were generated based on the CCD-RSM to analyze the effects of the individual parameters and their interactions.

3.1.2 Analysis of Variance (ANOVA) and Model Fitting

The results of the response surface regressions in the form of ANOVA for separation efficiency η , pressure drop ΔP , and quality factor q are presented in Tables 4–6. The fitting results and reliability of the three models were verified based on their high F -values and low p -values. The F -value was calculated based on the ratio of two variances or two mean squares, with larger values representing a greater significance of the model. Tables 4–6 show that the values of R^2 and $Adj.R^2$ are close to 1, and

Table 4 Analysis of variance for the separation efficiency

Source	Sum of squares	Df	Mean square	F-value	p-value	Remarks
Quadratic model	112.72	14	8.05	34.19	< 0.0001	significant
A-D _H	0.4718	1	0.4718	2.00	0.1774	
B-D _S	43.42	1	43.42	184.40	< 0.0001	significant
C-B _S	1.98	1	1.98	8.43	0.0109	significant
D-B _H	6.10	1	6.10	25.89	0.0001	significant
AB	13.98	1	13.98	59.37	< 0.0001	significant
AC	0.3724	1	0.3724	1.58	0.2278	
AD	1.48	1	1.48	6.29	0.0241	significant
BC	1.77	1	1.77	7.52	0.0151	significant
BD	0.1053	1	0.1053	0.4473	0.5138	
CD	2.64	1	2.64	11.23	0.0044	significant
A ²	1.53	1	1.53	6.51	0.0221	significant
B ²	12.86	1	12.86	54.60	< 0.0001	significant
C ²	18.05	1	18.05	76.65	< 0.0001	significant
D ²	2.27	1	2.27	9.63	0.0073	significant
Residual	3.53	15	0.2355			
Lack of Fit	3.16	10	0.3164			

R²=96.96%; Adj.R²=94.13%; Pred.R²=83.87%; Adeq Precision=26.9536

Table 5 Analysis of variance for the pressure drop

Source	Sum of squares	Df	Mean square	F-value	p-value	Remarks
Quadratic model	18353.93	14	1310.99	54.31	< 0.0001	significant
A-D _H	6867.61	1	6867.61	284.49	< 0.0001	significant
B-D _S	2184.96	1	2184.96	90.51	< 0.0001	significant
C-B _S	1845.96	1	1845.96	76.47	< 0.0001	significant
D-B _H	0.0323	1	0.0323	0.0013	0.9713	
AB	887.90	1	887.90	36.78	< 0.0001	significant
AC	229.26	1	229.26	9.50	0.0076	significant
AD	313.67	1	313.67	12.99	0.0026	significant
BC	0.1293	1	0.1293	0.0054	0.9426	
BD	142.42	1	142.42	5.90	0.0282	significant
CD	218.67	1	218.67	9.06	0.0088	significant
A ²	1622.90	1	1622.90	67.23	< 0.0001	significant
B ²	3190.46	1	3190.46	132.17	< 0.0001	significant
C ²	2066.26	1	2066.26	85.60	< 0.0001	significant
D ²	993.27	1	993.27	41.15	< 0.0001	significant
Residual	362.10	15	24.14			
Lack of Fit	317.70	10	31.77			

R²=98.07%; Adj.R²=96.26%; Pred.R²=89.88%; Adeq Precision=21.5765

the difference between them is minimal, indicating model accuracy. The *p*-value of the term is less than 0.05, indicating that it significantly affects the response indicator. As shown in Tables 4–6, except for terms A, AC, and BD, *p*-values for the other terms are less than 0.05, indicating a significant effect on separation efficiency. Moreover, a similar situation exists for the pressure drop; the *p*-values of the other terms, except for D and BC, are less than 0.05. Additionally, *p*-values of terms other than AC, BD, and CD are less than 0.05 for the quality factor. Simplified regression equations based on the significant terms are shown in Eqs. (16–18):

$$\eta (\%) = 81.44 - 1.35B - 0.2875C - 0.5040D + 0.9348AB - 0.3043AD - 0.3327BC - 0.4065CD - 0.2364A^2 - 0.6847B^2 + 0.8112C^2 + 0.2875D^2 \tag{17}$$

$$\Delta P (\text{Pa}) = 617.18 + 16.92A - 9.54B + 8.77C + 7.45AB + 3.79AC + 4.43AD + 2.98BD - 3.70CD + 7.69A^2 + 10.79B^2 + 8.68C^2 + 6.02D^2 \tag{18}$$

Table 6 Analysis of variance for the quality factor

Source	Sum of squares	Df	Mean square	F-value	p-value	Remarks
Quadratic model	0.8532	14	0.0609	52.95	<0.0001	significant
A-D _H	0.0965	1	0.0965	83.85	<0.0001	significant
B-D _S	0.1417	1	0.1417	123.11	<0.0001	significant
C-B _S	0.0837	1	0.0837	72.70	<0.0001	significant
D-B _H	0.0348	1	0.0348	30.22	<0.0001	significant
AB	0.0391	1	0.0391	33.98	<0.0001	significant
AC	3.940E-06	1	3.940E-06	0.0034	0.9541	
AD	0.0280	1	0.0280	24.35	0.0002	significant
BC	0.0099	1	0.0099	8.58	0.0104	significant
BD	0.0002	1	0.0002	0.1737	0.6827	
CD	0.0052	1	0.0052	4.51	0.0508	
A ²	0.0493	1	0.0493	42.81	<0.0001	significant
B ²	0.3001	1	0.3001	260.74	<0.0001	significant
C ²	0.0406	1	0.0406	35.28	<0.0001	significant
D ²	0.0010	1	0.0010	0.9089	0.3555	
Residual	0.0173	15	0.0012			
Lack of Fit	0.0153	10	0.0015			

R²=98.02%; Adj.R²=96.17%; Pred.R²=89.54%; Adeq Precision=35.1848

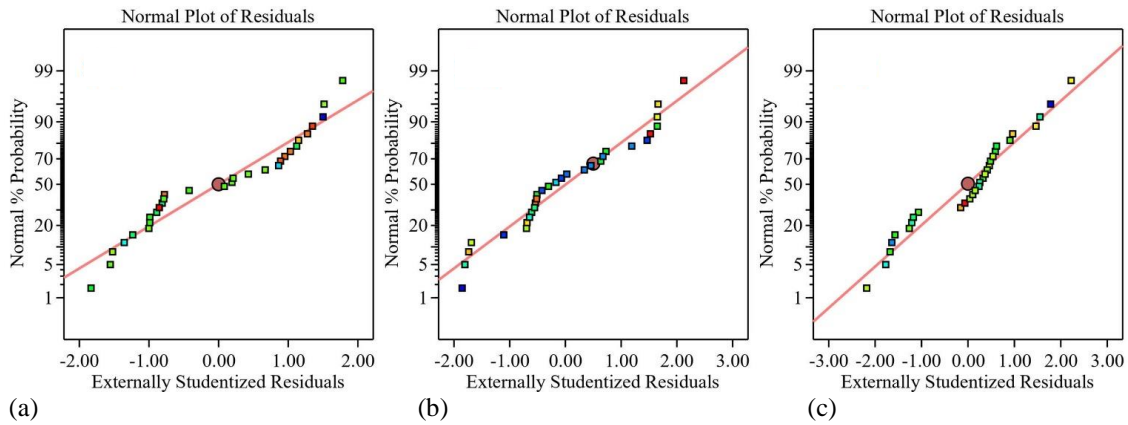


Fig. 4 Normal probability plots: (a) separation efficiency, (b) pressure drop and (c) quality factor

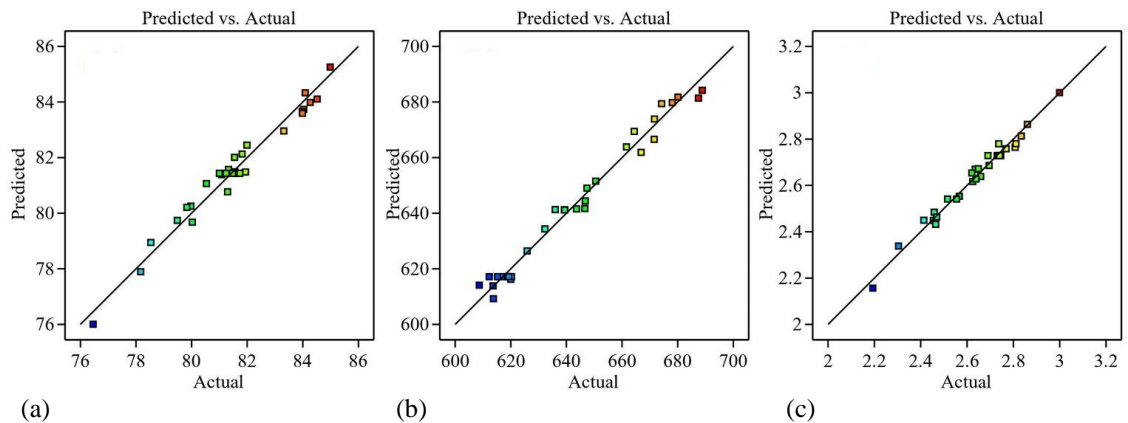
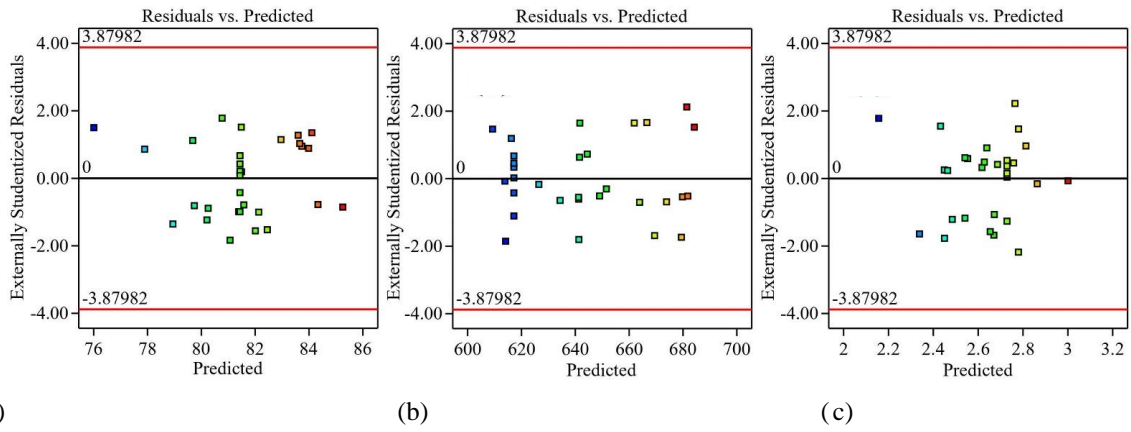


Fig. 5 Predicted versus actual plots: (a) separation efficiency, (b) pressure drop and (c) quality factor

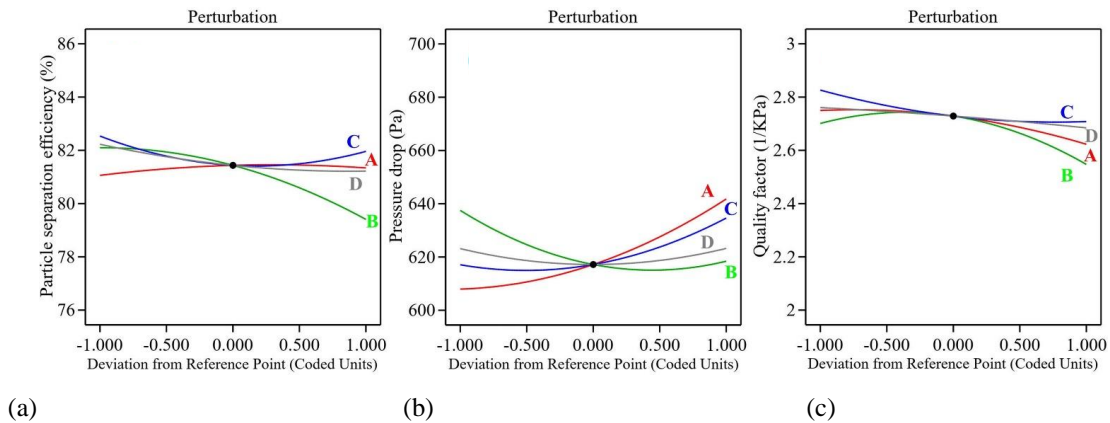
$$\begin{aligned}
 q \text{ (1/KPa)} = & 2.72 - 0.0634A - 0.0768B - 0.0590C \\
 & - 0.0381D + 0.0494AB - 0.0419AD - 0.0248BC \\
 & - 0.0415A^2 - 0.1037B^2 + 0.0394C^2
 \end{aligned}
 \tag{19}$$

The adequacy of the quadratic model was determined by applying diagnostic plots. Figure 4 shows normal

probability plots for separation efficiency, pressure drop, and quality factor. Most of the residuals fall within a straight line, indicating the satisfactory adequacy of the regression models for all responses. Figure 5 also shows that all points are close to the diagonal line, demonstrating a high correlation between predicted and actual values,



(a) (b) (c)
Fig. 6 Residual versus predicted response plots: (a) separation efficiency, (b) pressure drop and (c) quality factor



(a) (b) (c)
Fig. 7 Perturbation plots: (a) separation efficiency, (b) pressure drop and (c) quality factor

and the regression models are found to be valid and significant. Moreover, as shown in Fig. 6, all points are randomly distributed within a residual range of ± 3.87982 . This confirms that the proposed models are adequate.

A perturbation plot was used to compare the effects of the parameters on the responses. Figure 7 shows the different deviation levels of the parameters with respect to the separation efficiency, pressure drop, and quality factor. It is evident from Fig. 7(a) that line B has a higher divergence from the reference point, indicating that the apex cone bottom length D_S has a greater influence on separation efficiency than other parameters. Conversely, line A demonstrates minimal deviation, indicating that the vortex stabilizer diameter D_H is the least sensitive to the separation efficiency response compared to the apex cone height B_H and position B_S . A perturbation plot of the pressure drop with respect to the four parameters investigated is shown in Fig. 7(b). Except for line D, the other lines show significant divergence from the reference point, implying that D_H , D_S , and B_S contribute to the pressure drop. Additionally, the divergence level of line A is the highest, followed by lines B and C, indicating that the influences of D_H , D_S , and B_S on pressure drop decreases. Figure 7(c) shows a perturbation plot of the quality factor for the four parameters. According to the deviation level, these parameters can be ranked in the following descending order of influence: D_S , D_H , B_S , and B_H .

3.2 Analysis of Response Surfaces

3.2.1 Effects of Different Parameters on Separation Efficiency

The effects of the vortex stabilizer diameter D_H , apex cone bottom length D_S , position B_S , and height B_H on separation efficiency are shown in Fig. 8. As shown in Fig. 8(a), the relationship between D_H and separation efficiency is represented by a line of slight variation, indicating that a change in D_H has little effect on separation efficiency. The difference between the maximum and minimum separation efficiencies in the D_H range is approximately 1%. As presented in Fig. 8(b), separation efficiency initially increases but subsequently decreases with an increase in D_S from 65.45 to 157.85 mm. This can be attributed to the reduced turbulence intensity near the apex cone, which stabilizes the internal flow field and reduces particle back-mixing by increasing D_S from 65.45 to 88.55 mm. The fact that separation efficiency decreases as D_S increases further suggests that the effective passing area decreases, preventing particles from entering the dust box and allowing more particles to escape from the outlet. Figure 8(c) illustrates the effect of B_S on separation efficiency, where separation efficiency decreases as B_S increases from -80.85 to -26.95 mm, a larger recirculation area in the dust box is achieved, which leads to more particles entering the central vortex and escaping with the up flow. As B_S increases to 26.95 mm, owing to the increased passing area, more particles are

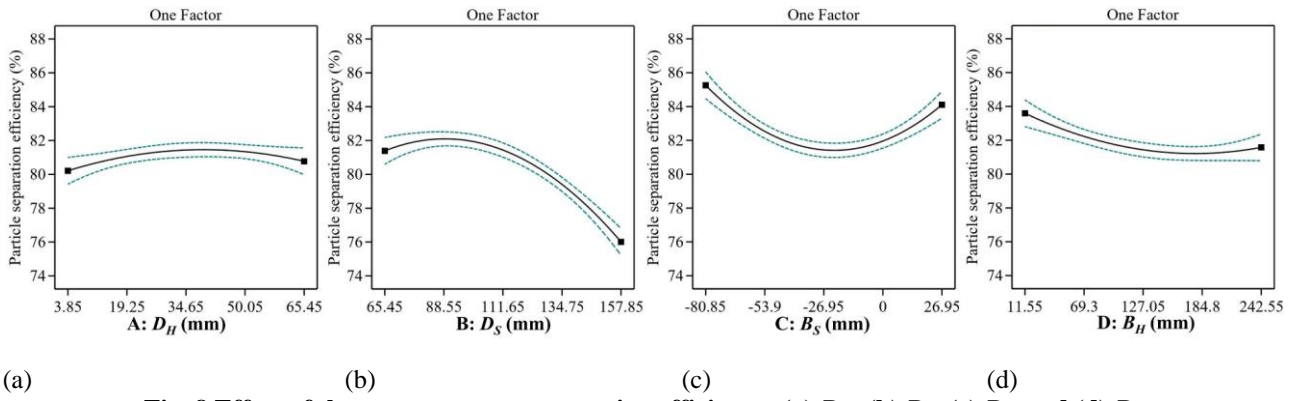


Fig. 8 Effect of the parameters on separation efficiency: (a) D_H , (b) D_S , (c) B_S , and (d) B_H

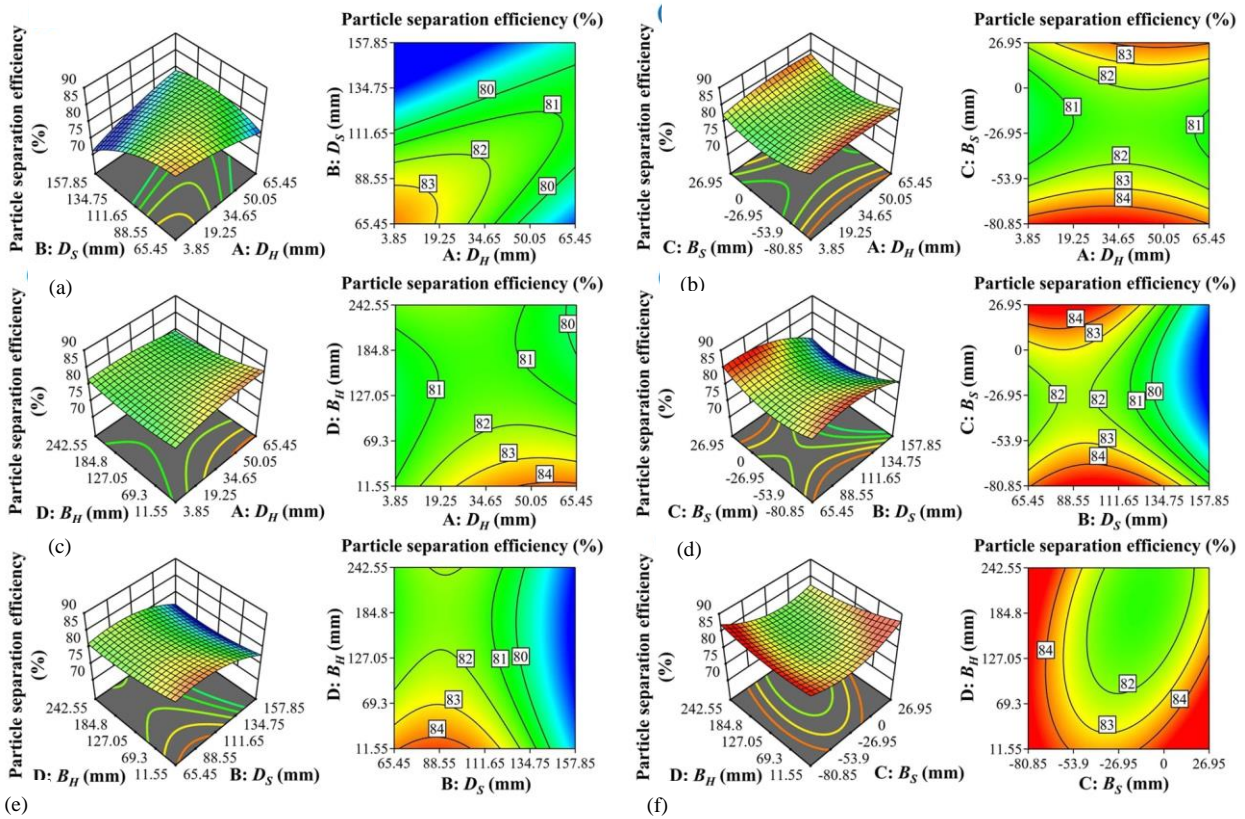


Fig. 9 3D response surface and contour plots for separation efficiency: (a) D_H and D_S , (b) D_H and B_S , (c) D_H and B_H , (d) D_S and B_S , (e) D_S and B_H , and (f) B_S and B_H

allowed to enter the dust box along the cyclone wall and then collect, thereby increasing separation efficiency. The effect of B_H on separation efficiency is shown in Fig. 8(d). When B_H increases from 11.55 to 127.05 mm, the enlarged surface area of the apex cone results in greater particle accumulation, and the possibility of particles escaping with the up flow increases. Therefore, separation efficiency is reduced. However, a further increase in B_H leads to a minimal increase in separation efficiency, indicating that a larger B_H promotes a drop of particles on the surface of the apex cone, which is beneficial for the particles to fall into the dust box.

Figure 9 shows the interaction effects of the combined parameters on separation efficiency using 3D response surface and contour plots. Each plot illustrates the interactions between the parameters affecting the

separation efficiency while maintaining other parameters constant at the central level (0). Figures 9(a–c) describe the interaction between D_H and the other three parameters, D_S , B_S , and B_H , on separation efficiency. Notably, D_S emerges as the most influential variable for separation efficiency; as D_S increases from 65.45 to 157.85 mm, separation efficiency decreases from 82% to 71% in Fig. 9(a), while concerning D_H increases from 3.85 to 65.45 mm, separation efficiency also decreases slightly. The 3D graph indicates that the interaction between D_H and D_S produces the highest separation efficiency of 83% at $D_H = 3.85$ mm and $D_S = 65.45$ mm. Figure 9(b) shows that as B_S increases from -80.85 to 26.95 mm, separation efficiency initially decreases and then increases, and the highest separation efficiency of 85% can be observed when B_S is -80.85 mm. However, for a given B_S value, variation in

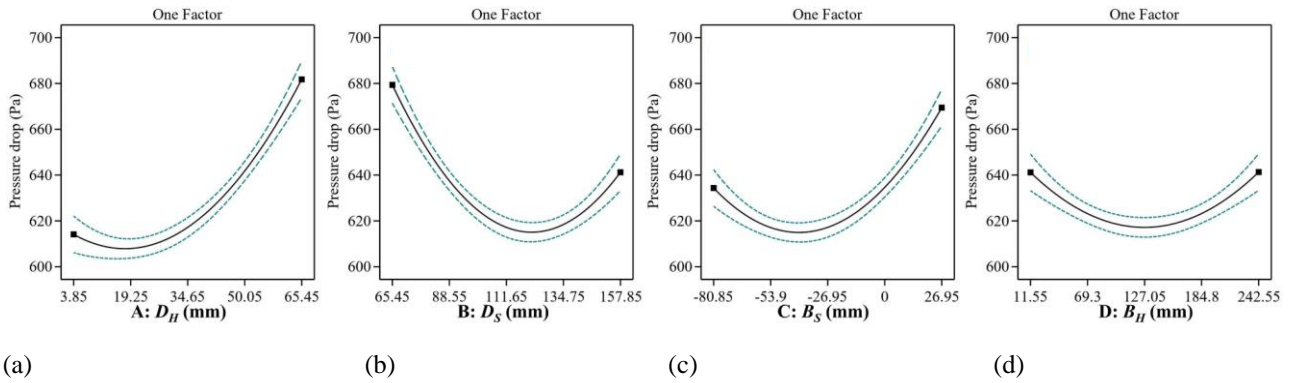


Fig. 10 Effect of the parameters on pressure drop: (a) D_H , (b) D_S , (c) B_S , and (d) B_H

separation efficiency is minimal as D_H changes. Figure 9(c) reveals that as D_H increases, separation efficiency exhibits a slight declining trend. However, separation efficiency is almost unaffected by B_H . Notably, the highest separation efficiency can be attained at $B_H = 11.55$ mm and $D_H = 65.45$ mm. The effects of the interactions between the other parameters on separation efficiency are shown in Figs. 9(d–f). Figure 9(d) shows the correlation between D_S and B_S . The effect of D_S on separation efficiency is substantial when B_S is -26.95 mm, but its influence diminishes at other values. When D_S ranges from 65.45 to 111.65 mm, the highest separation efficiency of 84% is obtained when $B_S = -80.85$ or 26.95 mm, with the lowest separation efficiency at $B_S = -26.95$ mm. The graph depicted in Fig. 9(e) shows that the increase in B_H causes a slight decrease in separation efficiency only when $D_S = 65.45$ – 111.65 mm; in the remaining cases, separation efficiency is almost constant. Moreover, as D_S increases, separation efficiency gradually diminishes. Figure 9(f) exhibits a hyperbolic trend for separation efficiency with increasing both B_S and B_H . Under both scenarios, separation efficiency initially decreases and then gradually increases. When B_S approaches zero, a higher B_H value decreases separation efficiency.

3.2.2 Effects of Different Parameters on Pressure Drop

Figure 10 illustrates the individual influences of four parameters: vortex stabilizer diameter D_H , apex cone bottom length D_S , position B_S , and height B_H on pressure drop. As shown in Fig. 10(a), as D_H increases from 3.85 to 19.25 mm, the reduction in the radial pressure gradient results in an improved flow and a decrease in pressure drop. However, a further increase in D_H to 65.45 mm leads to an increase in pressure drop, probably owing to an increase in the vortex stabilizer wall area, which results in increased friction with the gas, thereby increasing dissipation loss. Figure 10(b) depicts the effect of D_S on pressure drop; as D_S increases from 65.45 to 111.65 mm, the tangential velocity of gas decreases near the apex cone, thereby enhancing flow stability and reducing the pressure drop by 60 Pa. However, a higher D_S can reduce the effective passing area and intensify the flow oscillation, eventually leading to an increase in pressure drop. Figure 10(c) illustrates the effect of the B_S on pressure drop. As B_S increases from -80.85 to -26.95 mm, the internal flow field tends to stabilize, and less energy is lost; thus, pressure drop decreases. However, when B_S increases to 26.95 mm, a higher pressure drop is observed. This is

mainly owing to the reduced flow area near the cone, where turbulence loss intensifies. A minimal variation in pressure drop with changes in B_H can be observed in Fig. 10(d). This indicates that the effect of B_H on pressure drop is insignificant, and the maximum and minimum values differ by approximately 20 Pa.

The combined effects of various parameters on pressure drop are illustrated in Fig. 11 using the 3D response surface and contour plots. Figure 11(a) shows the relationship between D_H and D_S . When D_H is between 3.85 and 19.25 mm, a substantial decrease in pressure drop can be observed when D_S values range from 111.65 to 157.85 mm. As D_H continues to increase to 65.45 mm, the pressure drop is the highest when D_S is at its maximum or minimum. The effects of D_H and B_S are illustrated in Fig. 11(b). Within the D_H range, most of the B_S values result in a lower pressure drop, particularly when B_S ranges from -53.9 to -26.95 mm, where the minimum pressure drop is 620 Pa. However, the pressure drop is higher for larger D_H (50.05 – 65.45 mm) and B_S (-26.95 – 26.95 mm). The effects of the D_H and B_H on the pressure drop in Fig. 11(c) are analogous to those in Fig. 11(b). A higher B_H within the D_H range results in a smaller pressure drop. The pressure drop is maximized when $D_H = 65.45$ mm. In Fig. 11(d), a hyperbolic trend can be observed for pressure drop. The increase in D_S and B_S initially leads to a decrease in pressure drop, which then gradually increases. The lowest pressure drop of approximately 620 Pa occurs at a D_S of approximately 111.65 mm and a B_S of approximately -53.9 mm. A similar phenomenon is evident in Figs. 11(e) and (f), where when B_H is maintained at 127.05 mm, D_S and B_S are 111.65 and -53.9 mm, respectively, and the lowest pressure drop of 620 Pa is obtained.

3.2.3 Effects of Different Parameters on Quality Factor

The effects of the vortex stabilizer diameter D_H , apex cone bottom length D_S , position B_S , and height B_H on the quality factor are shown in Fig. 12. In Fig. 12(a), as D_H increases from 3.85 mm to approximately 19.25 mm, the quality factor initially increases, whereas it decreases for a larger D_H . This can be attributed to the negligible effect of D_H on separation efficiency. Conversely, a smaller D_H results in a lower pressure drop, whereas pressure drop increases as D_H increases. Consequently, the variation in quality factor with respect to D_H is opposite to that of pressure drop. An analogous change is evident for D_S in Fig. 12(b). The highest quality factor, approximately 2.75 $1/\text{KPa}$, is attained between 88.55 and 111.65 mm.

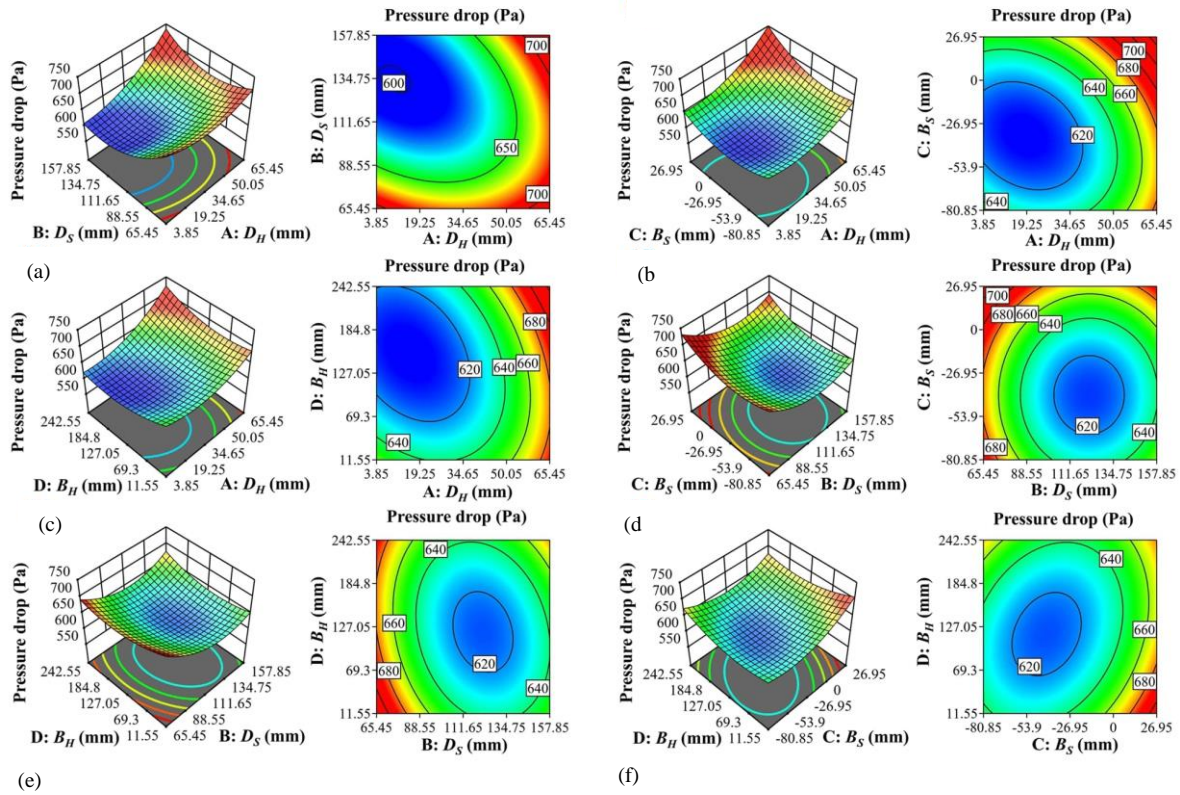


Fig. 11 3D response surface and contour plots for pressure drop: (a) D_H and D_S , (b) D_H and B_S , (c) D_H and B_H , (d) D_S and B_S , (e) D_S and B_H , and (f) B_S and B_H

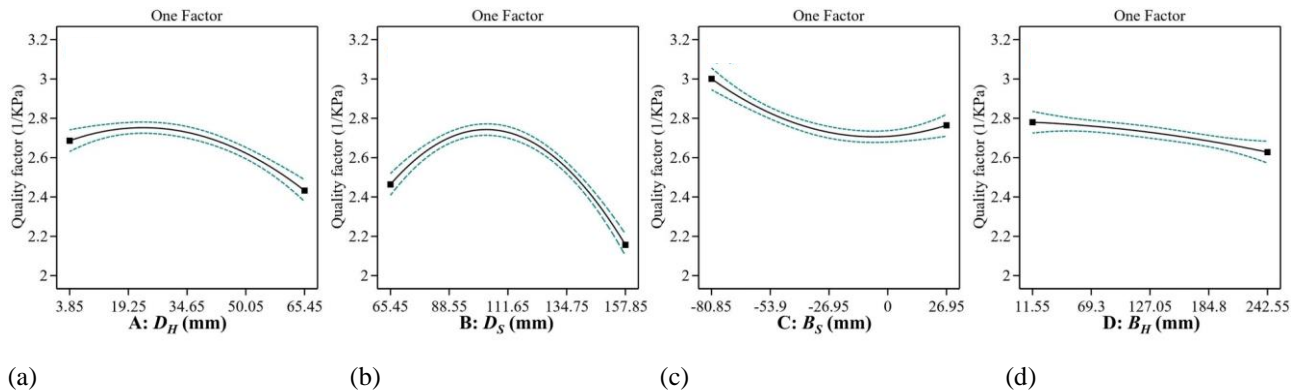


Fig. 12 Effect of the parameters on quality factor: (a) D_H , (b) D_S , (c) B_S , and (d) B_H

Moreover, the effect of D_S is more pronounced than that of D_H , where the difference between the maximum and minimum quality factors reaches approximately 0.6 1/KPa, compared with 0.3 1/KPa for D_H . Fig. 12(c) shows that B_S should be minimized; specifically, the closer the apex cone is to the bottom of the dust box, the more optimal the overall separation performance. This is attributed to the fact that a higher separation efficiency and lower pressure drop can be achieved simultaneously when B_S approaches -80.85 mm. Although a high separation efficiency is achieved when B_S reaches 26.95 mm, it leads to an increased pressure drop. According to Fig. 12(d), the effect of B_H on the quality factor is minimal, with the difference between the maximum and minimum quality factors being only 0.1 1/KPa. This is attributed to the negligible effect of B_H on separation efficiency, with a

maximum difference of only 2%. Furthermore, its effect on pressure drop is negligible, with a maximum variation of 20 Pa.

The 3D response surface and contour plots in Fig. 13 illustrate the interactions between the four parameters and the quality factor. In Fig. 13(a), a hyperbolic trend is evident for the quality factor. In both scenarios, the quality factor initially increases and subsequently decreases. The quality factor reaches 2.6 1/KPa when D_H falls within the 3.85–19.25 mm range and D_S within the 88.55–111.65 mm range. Figure 13(b) illustrates the combined interaction between the D_H and B_S . For a given B_S , varying D_H from 3.85 to 65.45 mm has no obvious effect on the quality factor and can achieve a substantial quality factor at a B_S of -80.85 mm; particularly, when D_H is close to 19.25 mm, the quality factor reaches a maximum of 3 1/KPa. In Fig.

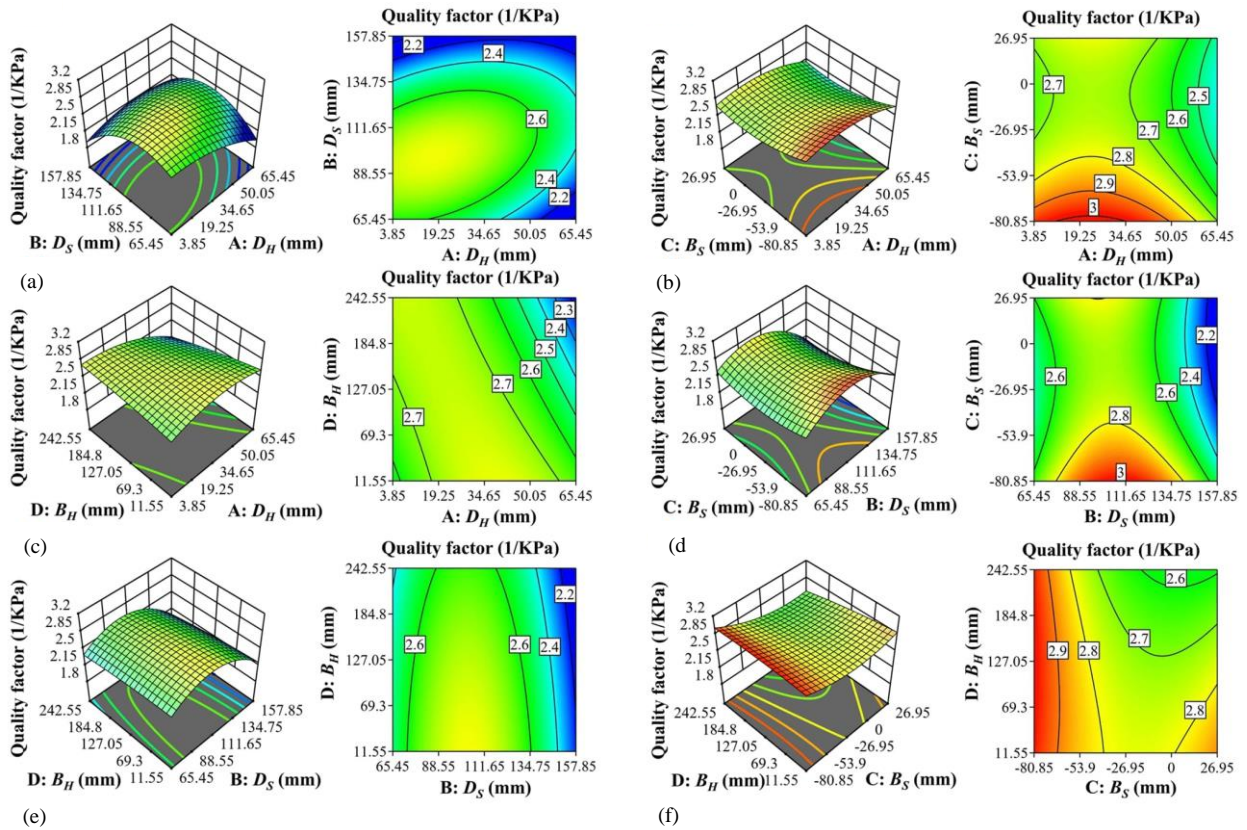


Fig. 13 3D response surface and contour plots for quality factor: (a) D_H and D_S , (b) D_H and B_S , (c) D_H and B_H , (d) D_S and B_S , (e) D_S and B_H , and (f) B_S and B_H

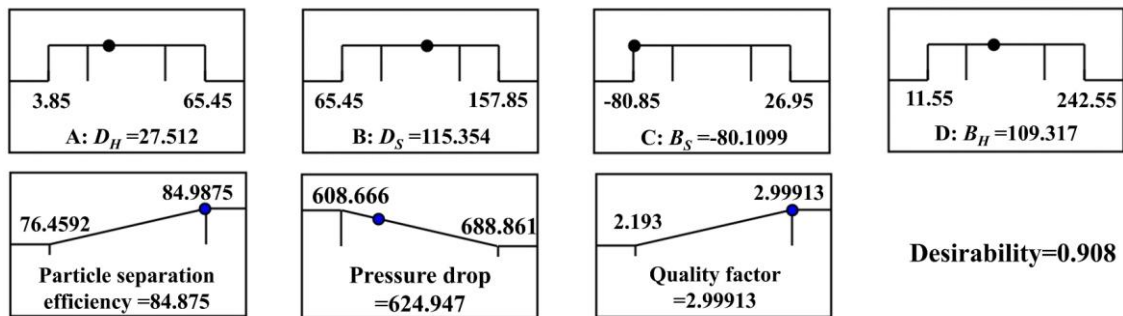


Fig. 14 Desirability values for numerical optimization of four parameters

13(c), the quality factor reaches approximately 2.7 1/KPa when D_H ranges between 19.25 and 50.05 mm, but the quality factor exhibits minimal variation with B_H . As B_H approaches 242.55 mm, the change in D_H significantly impacts the quality factor. As shown in Fig. 13(d), as D_S increases from 65.45 to 157.85 mm, the quality factor initially increases and then decreases. Furthermore, with the increase in B_S from -80.85 to 26.95 mm, the change in quality factor is minimal. The quality factor reaches its highest value of about 3 1/KPa when D_S is 88.55–134.75 mm and B_S is at its minimum (-80.85 mm). When D_S approaches 157.85 mm, the quality factor is consistently very small, indicating that an excessively large D_S would significantly degrade performance. Figure 13(e) indicates that the quality factor initially increases before eventually declining as D_S increases from 65.45 to 157.85 mm. Notably, for a fixed D_S , the quality factor remains unchanged throughout the B_H range. Figure 13(f) reveals

that as B_S and B_H increases in range, the quality factor varies minimally and reaches the maximum when the apex cone is at the lower end ($B_S = -53.9$ to -80.85 mm).

3.3 Optimization

Numerical optimization was employed to assess the desirability of the overall model. Desirability is an objective metric that ranges from zero outside limits to one at the goal (Babaee et al., 2024). Desirability, with a value near 1.00, was considered optimal based on the results. A multi-objective optimization of four parameters was conducted using the desirability function approach to maximize the separation efficiency and quality factor of the cyclone and minimize pressure drop. The desirability values of the numerical optimization procedure are shown in Fig. 14, depicting the optimized conditions of separation efficiency = 84.875%, pressure drop = 627.947 Pa, and quality factor = 2.99913 1/KPa at $D_H = 27.512$ mm,

Table 7 Validation of the optimized structure

Results	Separation efficiency (%)	Pressure drop (Pa)	Quality factor (1/KPa)
Predicted	84.875	627.947	2.99913
Simulated	83.962	627.222	2.918

Table 8 Performance comparison between the original and optimized structures

Structure	Separation efficiency	Pressure drop	Quality factor
Original	79.506 %	621.567 Pa	2.501 1/KPa
Optimized	83.962 %	627.222 Pa	2.918 1/KPa
Difference	5.605 %	0.910 %	16.673 %

$D_S = 115.354$ mm, $B_S = -80.1099$ mm, and $B_H = 109.317$ mm with combined desirability of 0.908, indicating the applicability of the developed model.

A numerical simulation was performed under optimal conditions to evaluate the precision of the optimization procedure. Predicted and numerical results are listed in Table 7. The concordance between the two results validated the precision and capability of the model. Table 8 presents a comparison of performance before and after optimization, indicating that the separation efficiency increases from 79.506 to 83.962%, signifying an enhancement exceeding 5% relative to the original structure. Despite the optimized structure demonstrating a higher pressure drop, it increases merely from 621.567 to 627.222 Pa, reflecting an increase of only 0.9%. The quality factor, which serves as a comprehensive evaluation of cyclone performance, increases from 2.501 to 2.918 1/KPa, demonstrating an improvement of more than 16%. Consequently, the application of RSM optimization significantly improved the overall performance of the cyclone.

4. COMPARISON OF THE ORIGINAL AND OPTIMIZED STRUCTURES

4.1 Gas Phase

Figure 15(a) shows a comparison of static pressure contours of the original and optimized structures. In the optimized structure, static pressure increases slightly, which leads to a reduction in dynamic pressure and gas velocity, particularly at the cone tip and dust box. Consequently, the likelihood of particle remixing diminishes. On the other hand, the increase in static pressure further extends the length of the vortex, capturing the bottom vortex end to mitigate particle back-mixing and enhance separation efficiency (Zhang et al., 2023). Fig. 15(b) illustrates the distributions of turbulent viscosity for the two structures. Compared with the original structure, the region of high turbulent viscosity in the optimized structure near the cone tip and dust box is primarily concentrated on the surface of the combined internal components. With an increase in the effective passage area, turbulent viscosity in other regions decreases, which is advantageous for improving separation efficiency.

Figure 16 presents a comparison of velocity vectors of the original and optimized structures. An analysis of this figure reveals that the vortex end is attached to the

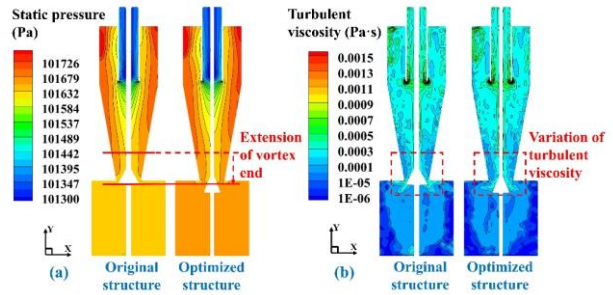


Fig. 15 Comparison of the (a) static pressure and (b) turbulent viscosity between the original and optimized structures

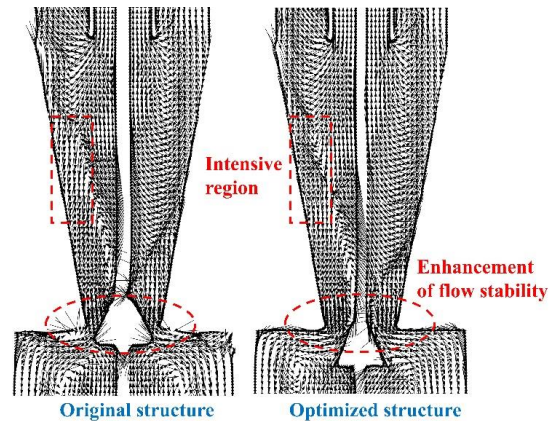


Fig. 16 Comparison of the velocity vectors between the original and optimized structures

apex cone, which may limit abduction and back-mixing of the particles positioned on the walls near the cone tip. In the optimized structure, the velocity vector in the middle of the cyclone separator cone is denser, resulting in an increased velocity that facilitates particle separation. The vortex end is positioned lower and further away from the wall, thereby enhancing flow stability. Furthermore, eddy currents in the region between the bottom of the cone and the top of the dust box are alleviated, which further aids in restraining particle back-mixing.

4.2 Particle Phase

Figure 17 compares particle trajectories of the original and optimized structures. The legend indicates different particle axial velocities. Descent distances L_1 , L_2 ,

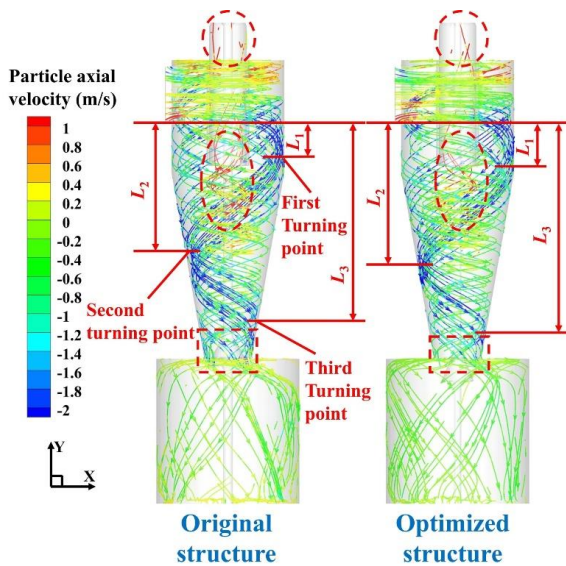


Fig. 17 Comparison of the particle trajectories between the original and optimized structures

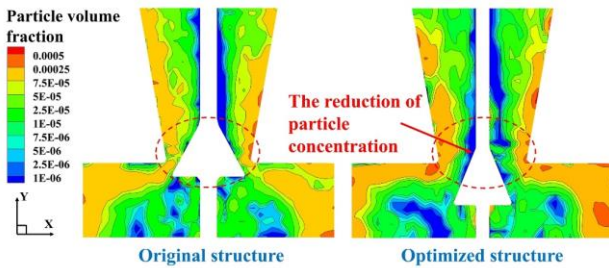


Fig. 18 Comparison of the particle volume fractions between the original and optimized structures

and L_3 are defined as the distances from the inlet bottom to the first, second, and third turning points, respectively. In the original structure, particle trajectories within the cyclone separator are more chaotic, resulting in increased particle separation times. Additionally, a greater number of particles escape with the up flow, whereas some particles become suspended at the top of the cylinder. Conversely, because of enhancements made to the internal components, L_1 , L_2 , and L_3 in the optimized structure are extended, promoting an increase in centrifugal force and kinetic energy of the particles, thereby improving separation efficiency. Additionally, the optimized structure facilitates a more orderly flow, leading to a reduction in the number of particles escaping with the central up flow.

Excessive particle aggregation at the cone tip hinders their flow and is particularly affected by the combined internal components. Therefore, an analysis of the particle volume fraction at cone tip and the apex cone area is essential. As illustrated in Fig. 18, the distance between the apex cone and wall surface in the original structure is insufficiently small, restricting the effective passage area. This limitation may significantly increase particle volume fraction in the cone-tip region, particularly along the wall of the vortex stabilizer and the apex cone. Additionally, it

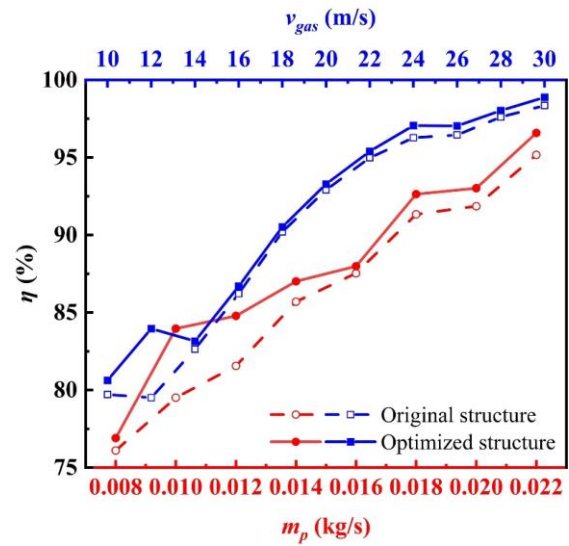


Fig. 19 Comparison of separation efficiencies between the original and optimized structures for different gas inlet velocities and particle inlet mass rates

can impede the sliding of particles into the dust box, thereby increasing the possibility of particle back-mixing. By contrast, the optimized structure reduces particle volume fraction on the wall of the combined internal components and provides a larger effective passage area for the particles, thereby facilitating their smooth entry into the dust box along the wall surface.

4.3 Separation Performance

4.3.1 Separation Efficiency

Figure 19 compares separation efficiencies of the original and optimized structures for various gas inlet velocities and particle inlet mass rates. Evidently, separation efficiency increases with higher gas inlet velocities and particle inlet mass rates. Additionally, the optimized structure exhibits an improved separation efficiency. This enhancement can be attributed to the capacity of the apex cone to capture the bottom vortex end of the optimized structure, which extends the vortex length and increases its distance from the wall. This configuration effectively reduces the diffusion and back-mixing of particles at the wall of the cone tip. Moreover, the optimized structure stabilizes the flow field and significantly mitigates the possibility of back-mixing caused by excessive particle aggregation, owing to the larger effective passing area.

4.3.2 Pressure Drop

Figure 20 shows a comparison of pressure drops between the original and optimized structures. Both structures exhibit a significant increase in pressure drop as the gas inlet velocity and particle inlet mass rate increase, whereas the variation in pressure drop with the particle mass flow rate is minimal. Essentially, the difference in pressure drop between the two structures is negligible. The optimized structure enhances the effective passing area at the cone tip and mitigates turbulence intensity, thereby reducing pressure drop. However, this optimization also results in increased contact between gas flow and

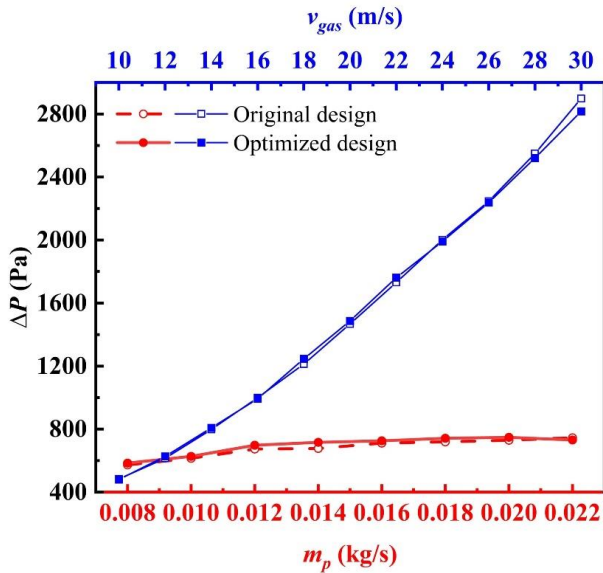


Fig. 20 Comparison of pressure drops between the original and optimized structures for different gas inlet velocities and particle inlet mass rates

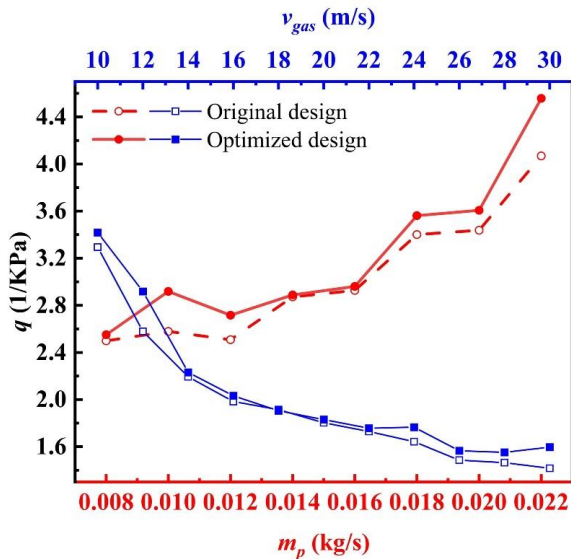


Fig. 21 Comparison of quality factors between the original and optimized structures for different gas inlet velocities and particle inlet mass rates

combined internal components, leading to a greater energy loss. Consequently, these two factors contribute to the pressure drop in the optimized structure, which is marginally higher than that in the original structure.

4.3.3 Quality Factor

Figure 21 illustrates the overall performance, measured in terms of quality factor, of both the original and optimized structures under varying gas inlet velocities and particle inlet mass rates. The quality factor is calculated using Eq. (16). As the gas inlet velocity increases, both the separation efficiency and pressure drop increase; however, a gradual decline in the quality factor can be observed, according to Eq. (16). A higher particle inlet mass rate enhances separation efficiency, whereas the increase in pressure drop is relatively modest, resulting

in an upward trend in quality factor. In both scenarios, the optimized structure exhibits significant advantages in terms of enhancing gas flow, reducing particle back-mixing, and facilitating particle separation.

5. CONCLUSION

In this study, multi-objective optimization was performed to determine the optimal geometric configurations of a cyclone with combined internal components, including a vortex stabilizer and an apex cone. Four parameters (vortex stabilizer diameter D_H , apex cone bottom length D_S , position B_S , and height B_H) were selected and their effects on separation efficiency, pressure drop, and quality factor were analyzed using RSM and CPF. The optimized structure was obtained using the desirability function approach, and the original and optimized structures were compared to assess the superiority of the optimized structure. The conclusions of this study are as follows:

- (1) According to ANOVA, D_S was the most significant parameter influencing separation efficiency and quality factor, whereas D_H exerted the greatest effect on pressure drop. Based on the original size of the combined internal components, the reduction in D_H and D_S enhanced separation efficiency and decreased pressure drop, resulting in a high quality factor. Additionally, lowering the position of the apex cone (reducing B_S) further contributed to improved performance.
- (2) When D_H , D_S , B_S and B_H were 27.512, 115.354, -80.1099, and 109.317 mm, respectively, the optimized structure increased separation efficiency, pressure drop, and quality factor by 5.605, 0.910, and 16.673%, respectively, compared to the original cyclone separator.
- (3) Compared with the original cyclone, the optimized separator exhibited a higher static pressure, resulting in a decrease in dynamic pressure and gas velocity, thereby minimizing particle back-mixing. Concurrently, the vortex end was positioned lower, and the wall turbulent viscosity diminished, both of which enhanced flow stability. In contrast, longer particle flow descent distances enhanced the centrifugal force and kinetic energy of the particles, whereas a larger effective passing area reduced particle volume fraction at the cone tip, which was conducive to improving separation efficiency.
- (4) Under various gas inlet rates and particle inlet mass rates, the optimized structure achieved a higher separation efficiency with only minor changes in pressure drop. Consequently, the overall performance, as measured by the quality factor, improved significantly.

ACKNOWLEDGEMENTS

The work was supported by the Natural Science Foundation of Jiangsu Province (Grant No. BK20230634), the Changzhou Key R&D Plan (Social Development

Technology Support) of China (Grant No. CE20225054), the Natural Science Foundation of Jiangsu Higher Education Institution of China (Grant No. 23KJB470001), the Research Startup Foundation of Changzhou University (Grant No. ZMF23020185).

CONFLICT OF INTEREST

The authors declare that they have no known competing financial interests or personal relationships that could have appeared to influence the work reported in this paper.

AUTHORS CONTRIBUTION

Zhen Zhang: Writing – review & editing, Methodology. **Haoran Qin:** Writing – original draft, Formal analysis. **Yujie Zhao:** Data curation, Investigation. **Lin Liu:** Writing – review & editing, Supervision, Methodology, Funding acquisition, Project administration. **Jing Li:** Supervision, Validation. **Haijun Pan:** Supervision, Validation. **Chenhui Hu:** Supervision, Investigation.

REFERENCES

- Altıok, E., Kaya, T. Z., Othman, N. H., Kınalı, O., Kitada, S., Güler, E., & Kabay, N. (2022). Investigations on the effects of operational parameters in reverse electro dialysis system for salinity gradient power generation using central composite design (CCD). *Desalination*, 525, 115508. <https://doi.org/10.1016/j.desal.2021.115508>
- Babae, S. A., Hosseini, M. S., & Hajizadeh, Y. (2024). Destruction of n-hexane from the air stream by pulsed discharge plasma: Modelling and key process parameters optimization by CCD-RSM. *Journal of Environmental Chemical Engineering*, 12(3), 112922. <https://doi.org/10.1016/j.jece.2024.112922>
- Bandara, J. C., Jayarathna, C., Thapa, R., Nielsen, H. K., Moldestad, B. M. E., & Eikeland, M. S. (2020). Loop seals in circulating fluidized beds – Review and parametric studies using CFPD simulation. *Chemical Engineering Science*, 227, 115917. <https://doi.org/10.1016/j.ces.2020.115917>
- Bandara, J. C., Thapa, R., Nielsen, H. K., Moldestad, B. M. E., & Eikeland, M. S. (2019). Circulating fluidized bed reactors - part 01: analyzing the effect of particle modelling parameters in computational particle fluid dynamic (CPFD) simulation with experimental validation. *Particulate Science and Technology*, 39(2), 223-236. <https://doi.org/10.1080/02726351.2019.1697773>
- Bumrunghthaichachan, E. (2023). A note of caution on numerical scheme selection: Evidence from cyclone separator CFD simulations with appropriate near-wall grid sizes. *Powder Technology*, 427, 118713. <https://doi.org/10.1016/j.powtec.2023.118713>
- Dehdarinejad, E., & Bayareh, M. (2023). Performance analysis of a novel cyclone separator using RBFNN and MOPSO algorithms. *Powder Technology*, 426, 118663. <https://doi.org/10.1016/j.powtec.2023.118663>
- Duan, J., Gao, S., Hou, C., Wang, W., Zhang, P., & Li, C. (2020). Effect of cylinder vortex stabilizer on separator performance of the Stairmand cyclone. *Powder Technology*, 372, 305-316. <https://doi.org/10.1016/j.powtec.2020.06.031>
- Elsayed, K., Parvaz, F., Hosseini, S. H., & Ahmadi, G. (2020). Influence of the dipleg and dustbin dimensions on performance of gas cyclones: An optimization study. *Separation and Purification Technology*, 239, 116553. <https://doi.org/10.1016/j.seppur.2020.116553>
- Feng, Y., Yuan, Z., Zhu, S., Zhang, M., & Yang, H. (2025). Numerical simulation of cold bubbling fluidized bed in thermochemical heat storage of carbide slag based on CFPD method. *Journal of Energy Storage*, 108, 115063. <https://doi.org/10.1016/j.est.2024.115063>
- Guo, M., Le, D. K., Sun, X., & Yoon, J. Y. (2022). Multi-objective optimization of a novel vortex finder for performance improvement of cyclone separator. *Powder Technology*, 410, 117856. <https://doi.org/10.1016/j.powtec.2022.117856>
- Guo, M., Lu, Y., Xue, C., Sun, X., & Yoon, J. Y. (2023). The impact of cylinder vortex stabilizer on fluctuating turbulence characteristics of a cyclone separator based on large eddy simulation. *Advanced Powder Technology*, 34(9), 104149. <https://doi.org/10.1016/j.apt.2023.104149>
- He, X., Liu, Q., Zhang, H., Kui, M., Tan, X., & Li, X. (2019). Numerical investigation of the performance of moisture separators based on two-way coupling model by Lagrangian-Eulerian methodology. *Annals of Nuclear Energy*, 124, 407-417. <https://doi.org/10.1016/j.anucene.2018.10.020>
- Jiang, S., Wang, X., Zhang, S., Wu, Q., Hou, L., & Qiao, X. (2024). Design and validation of a sampling module for a cyclonic wet-wall bioaerosol sampler using a computational fluid dynamics model. *Powder Technology*, 440, 119793. <https://doi.org/10.1016/j.powtec.2024.119793>
- Khalili, A. A. P., Vaziri, N. N. J., Kheradmand, S., & Khalili, A. A. D. (2023). A dimensional optimization study on cyclone performance under the oscillating boundary condition. *Chemical Engineering and Processing - Process Intensification*, 183, 109217. <https://doi.org/10.1016/j.cep.2022.109217>
- Kosaki, Y., Hirai, T., Yamanaka, Y., & Takeshima, K. (2015). Investigation on dust collection and particle classification performance of cyclones by airflow control for design of cyclones. *Powder Technology*, 277, 22-35. <https://doi.org/10.1016/j.powtec.2015.02.051>
- Kumar, V., & Jha, K. (2019). Multi-objective shape optimization of vortex finders in cyclone separators using response surface methodology and genetic algorithms. *Separation and Purification Technology*,

- 215, 25–31.
<https://doi.org/10.1016/j.seppur.2018.12.083>
- Li, J., Wang, T., Zhang, L., Chang, J., Song, Z., & Ma, C. (2020a). Multi-objective optimization of axial-flow-type gas-particle cyclone separator using response surface methodology and computational fluid dynamics. *Atmospheric Pollution Research*, *11*(9), 1487–1499.
<https://doi.org/10.1016/j.apr.2020.06.002>
- Li, Q., Wang, J., Xu, W., & Zhang, M. (2020b). Investigation on separation performance and structural optimization of a two-stage series cyclone using CPFD and RSM. *Advanced Powder Technology*, *31*(9), 3706–3714.
<https://doi.org/10.1016/j.apr.2020.07.006>
- Li, T., Sun, Z., Geng, K., Sun, M., & Wang, Z. (2023a). Numerical analysis of a novel cascading gas–liquid cyclone separator. *Chemical Engineering Science*, *270*, 118518.
<https://doi.org/10.1016/j.ces.2023.118518>
- Li, W., Huang, Z., & Li, G. (2023b). Improvement of the cyclone separator performance by the wedge-shaped roof: A multi-objective optimization study. *Chemical Engineering Science*, *268*, 118404.
<https://doi.org/10.1016/j.ces.2022.118404>
- Liang, H., Ma, J., Li, C., Mu, L., & Jiang, X. (2023). Study on the performance of downhole axial cyclone with spiral fins for drainage and sand removal. *Journal of Environmental Chemical Engineering*, *11*(5), 111032.
<https://doi.org/10.1016/j.jece.2023.111032>
- Liu, X., Zhang, H., Yang, H., Zhang, Y., & Lyu, J. (2023). Validation and evaluation of the CPFD modeling of dense particle flow velocity: Taking particle flow around an obstacle as an example. *Chemical Engineering Journal*, *453*, 139719.
<https://doi.org/10.1016/j.cej.2022.139719>
- Ma, Q., Lei, F., Xu, X., & Xiao, Y. (2017). Three-dimensional full-loop simulation of a high-density CFB with standpipe aeration experiments. *Powder Technology*, *320*, 574–585.
<http://dx.doi.org/10.1016/j.powtec.2017.07.094>
- Morin, M., Raynal, L., Reddy Karri, S. B., & Cocco, R. (2021). Effect of solid loading and inlet aspect ratio on cyclone efficiency and pressure drop: Experimental study and CFD simulations. *Powder Technology*, *377*, 174–185.
<https://doi.org/10.1016/j.powtec.2020.08.052>
- Pandey, S., & Brar, L. S. (2023). Performance analysis of cyclone separators with bulged conical segment using large-eddy simulation. *Powder Technology*, *425*, 118584.
<https://doi.org/10.1016/j.powtec.2023.118584>
- Shastri, R., Brar, L. S., & Elsayed, K. (2022). Multi-objective optimization of cyclone separators using mathematical modelling and large-eddy simulation for a fixed total height condition. *Separation and Purification Technology*, *291*, 120968.
<https://doi.org/10.1016/j.seppur.2022.120968>
- Tan, C., Hu, H., Ye, Q., E, D., Cui, J., Zhou, Z., Kuang, S., Zou, R., & Yu, A. (2024). Multi-objective optimization of hydrocyclones using meta-heuristic algorithms and preference-informed decision-making. *Powder Technology*, *444*, 120050.
<https://doi.org/10.1016/j.powtec.2024.120050>
- Tang, X., Yue, Y., & Shen, Y. (2023). Prediction of separation efficiency in gas cyclones based on RSM and GA-BP: Effect of geometry designs. *Powder Technology*, *416*, 118185.
<https://doi.org/10.1016/j.powtec.2022.118185>
- Vakamalla, T. R., & Mangadoddy, N. (2017). Numerical simulation of industrial hydrocyclones performance: Role of turbulence modelling. *Separation and Purification Technology*, *176*, 23–39.
<http://dx.doi.org/10.1016/j.seppur.2016.11.049>
- Venkatesh, S., Suresh Kumar, R., Sivapirakasam, S. P., Sakthivel, M., Venkatesh, D., & Yasar Arafath, S. (2020). Multi-objective optimization, experimental and CFD approach for performance analysis in square cyclone separator. *Powder Technology*, *371*, 115–129.
<https://doi.org/10.1016/j.powtec.2020.05.080>
- Wang, Z., Sun, G., Song, Z., Yuan, S., & Qian, Z. (2023). Effect of inlet volute wrap angle on the flow field and performance of double inlet gas cyclones. *Particuology*, *77*, 29–36.
<https://doi.org/10.1016/j.partic.2022.08.006>
- Wasilewski, M., & Brar, L. S. (2019). Effect of the inlet duct angle on the performance of cyclone separators. *Separation and Purification Technology*, *213*, 19–33.
<https://doi.org/10.1016/j.seppur.2018.12.023>
- Wasilewski, M., Brar, L. S., & Ligus, G. (2021). Effect of the central rod dimensions on the performance of cyclone separators - optimization study. *Separation and Purification Technology*, *274*, 119020.
<https://doi.org/10.1016/j.seppur.2021.119020>
- Wei, Q., Sun, G., & Gao, C. (2020). Numerical analysis of axial gas flow in cyclone separators with different vortex finder diameters and inlet dimensions. *Powder Technology*, *369*, 321–333.
<https://doi.org/10.1016/j.powtec.2020.05.038>
- Yang, H., Wang, N., Cao, Y., Meng, X., & Yao, L. (2023). Effects of helical fins on the performance of a cyclone separator: A numerical study. *Advanced Powder Technology*, *34*(1), 103929.
<https://doi.org/10.1016/j.apr.2022.103929>
- Yang, J., Dong, Z., Shen, C., Zhang, W., Hao, X., & Guan, G. (2019). Analysis of effect of radial confluence flow on vortex core motion. *Powder Technology*, *356*, 871–879.
<https://doi.org/10.1016/j.powtec.2019.09.013>
- Yao, Y., Huang, W., Wu, Y., Zhang, Y., Zhang, M., Yang, H., & Lyu, J. (2021). Effects of the inlet duct length on the flow field and performance of a cyclone separator with a contracted inlet duct. *Powder Technology*, *393*, 12–22.
<https://doi.org/10.1016/j.powtec.2021.07.044>

- Yao, Y., Shang, M., Ke, X., Huang, Z., Zhou, T., & Lyu, J. (2024). Effects of the inlet particle spatial distribution on the performance of a gas-solid cyclone separator. *Particuology*, 85, 133–145. <https://doi.org/10.1016/j.partic.2023.03.024>
- Zhang, H., Li, W., Ma, Q., Zhang, Y., & Lei, F. (2020). Numerical study on influence of exit geometry in gas–solid flow hydrodynamics of HDCFB riser by CPFD. *Advanced Powder Technology*, 31(9), 4005-4017. <https://doi.org/10.1016/j.apt.2020.08.006>
- Zhang, R., Yang, J., Han, S., Hao, X., & Guan, G. (2023). Improving advantages and reducing risks in increasing cyclone height via an apex cone to grasp vortex end. *Chinese Journal of Chemical Engineering*, 54, 136–143. <https://doi.org/10.1016/j.cjche.2022.04.014>
- Zheng, Y., Liu, X., & Ni, L. (2022). Numerical investigation on particles separation using an enhanced cyclone with shunt device: Effect of vortex finder lengths. *Chemical Engineering and Processing - Process Intensification*, 181, 109125. <https://doi.org/10.1016/j.cep.2022.109125>